AIAA SciTech Forum
6-10 January 2020, Orlando, FL
AIAA Scitech 2020 Forum

10.2514/6.2020-2240

Numerical Stability Investigation of Inward Radial Rayleigh-Bénard-Poiseuille Flow

M. K. Hasan* and A. Gross†

Mechanical and Aerospace Engineering Department, New Mexico State University, Las Cruces, NM 88003

Inward radial Rayleigh-Bénard-Poiseuille flow can exhibit a buoyancy-driven instability when the Rayleigh number exceeds a critical value. Furthermore, similar to plane Rayleigh-Bénard-Poiseuille flow, a viscous Tollmien-Schlichting instability can occur when the Reynolds number is high enough. Direct numerical simulations were carried out with a compressible Navier-Stokes code in cylindrical coordinates to investigate the spatial stability of the inward radial flow inside the collector of a hypothetical solar chimney power plant. The convective terms were discretized with fifth-order-accurate upwind-biased compact finite-differences and the viscous terms were discretized with fourth-order-accurate compact finite differences. For cases with buoyancy-driven instability, steady three-dimensional waves are strongly amplified. The spatial growth rates vary significantly in the radial direction and lower azimuthal mode numbers are amplified closer to the outflow. Traveling oblique modes are amplified as well. The growth rates of the oblique modes decrease with increasing frequency. In addition to the purely radial flow, a spiral flow with swept inflow was examined. Overall lower growth rates are observed for the spiral flow compared to the radial flow. Different from the radial flow, the relative wave angles and growth rates of the left and right traveling oblique modes are not identical. A plane RBP case with viscosity-driven instability by Chung et al. was considered as well. The reported growth rate and phase speed were matched with good accuracy.

I. Introduction

The increasing demand for clean renewable energy has led to the development of many novel electrical power generation concepts such as the solar chimney power plant (SCPP). The SCPP represents an entire sustainable energy pathway from solar energy to electrical power. It has three major components which are referred to as collector, turbine and chimney. The operating principle is relatively simple compared to the conventional coal or gas power plants. The air under the collector is heated by the ground and accelerates towards the collector center, where it passes through turbines and then escapes through the central chimney. What makes the SCPP attractive is that the generated power scales with the product of collector area and chimney height.[1] A solar chimney power plant designed by Schlaich, Bergermann and Partner in Manzanares, Spain successfully produced approximately 50kW of electrical power from 1982 to 1989.[1–4] According to Schlaich,[1] the available electrical power can be estimated from

$$P = \eta_c \eta_t \frac{2}{3} g \frac{H_t \pi R_c^2 I}{c_p T_\infty}\,, \tag{1}$$

where η_c and η_t are the collector and turbine efficiency, g is the gravitational acceleration, I is the solar irradiation, and T_∞ is the ambient temperature. The generated power scales with the collector area, πR_c^2 and the chimney height, H_t.

The radial flow inside the collector is subjected to a vertical temperature gradient which results in a buoyancy acceleration that is opposed by a gravitational acceleration. Such flows are referred to as Rayleigh-Bénard-Poiseuille (RBP) flows. Both the buoyancy- and viscosity-driven instability of plane (i.e. not radial)

*Graduate Research Assistant. Member AIAA.
†Associate Professor. Associate Fellow AIAA.

RBP flows have been investigated in detail. The onset of flow instability is governed by two dimensionless numbers which are the Reynolds number,

$$Re = \frac{u_{max} h/2}{\nu}\,, \tag{2}$$

with maximum velocity, u_{max}, channel height, h, and kinematic viscosity, ν, and the Rayleigh number,

$$Ra = \frac{g h^3 \gamma \Delta T}{\nu \alpha}\,, \tag{3}$$

with gravitational acceleration, g, volumetric thermal expansion coefficient, γ, temperature difference, ΔT, and thermal diffusivity, α. Miles[5] studied the effect of stratification on the stability of inviscid, incompressible and parallel flows. Pearlstein[6] observed that either two-dimensional (2-D) or three-dimensional (3-D) waves are the most unstable modes of instability in plane RBP flows. Gage and Reid[7] first investigated the linear temporal stability of plane RBP flows and established the stability boundaries for the onset of both buoyancy and viscosity-driven instability. When the Reynolds number is below Re_c=5,400 and the Rayleigh number is above Ra_c=1,708, buoyancy-driven instability occurs and 3-D waves with a wave angle of 90deg are most amplified. For $Re > Re_c$ and $Ra < Ra_c$ viscosity-driven instability arises and 2-D Tollmien-Schlichting (T-S) waves with a wave angle of 0deg are most amplified. The stability results for plane RBP flow by Gage and Reid[7] were confirmed by various numerical and experimental studies. The forced convective heat transfer between horizontal flat plates was investigated by Mori and Uchida.[8] Counter-rotating longitudinal vortices were found to be the dominant disturbance mode when the temperature difference between the plates was increased above a certain threshold. Below a critical Reynolds number ($Re < Re_c$), the flow was found to become unstable and longitudinal vortex rolls developed, provided that the Rayleigh number was high enough and the spanwise extent of the channel was infinite. A linear stability analysis by Fujimura and Kelly[9] revealed that for a certain low Reynolds number range ($0.01 \le \mathrm{Re} \le 100$), the critical Rayleigh number for 2-D unstable waves was increasing with Reynolds number. This finding is essentially consistent with the zero degree wave angle neutral curve by Gage and Reid.[7]

The flow inside the collector of SCPPs constitutes an inward radial RBP flow. Such flows have attracted far less attention than plane RBP flows. For the inward radial channel flow, the flow accelerates strongly in the streamwise direction because of continuity ($\rho v \propto 1/r$-relationship) and non-parallel effects become important. Since acceleration generally has a stabilizing effect,[10] the inward radial RBP flow is expected to be more stable than the plane RBP flow especially near the collector outlet where the acceleration is very large. Also, different from plane RBP flow, only certain azimuthal wavelengths are possible for radial RBP flows. The detailed understanding of the primary and secondary instabilities of inward radial RBP flows appears crucial for the successful design and operation of SCPP plants. Of particular interest are the critical parameters (such as Reynolds number, Rayleigh number, Prandtl number) that determine if and where coherent flow structures will develop. Coherent flow structures modify the overall heat transfer and pressure drop in the collector and thus will have a profound effect on the SCPP performance.

Because it is considered a technically and economically feasible sustainable and renewable energy alternative, the SCPP technology has attracted considerable attention in the scientific literature. Bernardes et al.[11] performed computational analyses of natural radial laminar flows with solar energy addition for five distinctive geometric configurations such as a straight, curved and slanted junction as well as a conic chimney and curved junction/diffuser. The thermo-hydrodynamic properties, such as the temperature fields, recirculation, and mass flow rate were analyzed. Ming et al.[12–14] carried out Reynolds-averaged Navier-Stokes (RANS) calculations to investigate the effect of crosswind on the performance and efficiency of SCPPs. Using the Manzanares prototype as a reference model, Pastohr et al.[15] performed numerical analyses based on RANS calculations and observed that the efficiency of SCPPs is strongly influenced by the mass flow rate and the pressure difference across the turbines. Xu et al.[16] investigated numerically how the generated power and energy losses of the SCPP system are affected by the solar radiation and turbine efficiency. Based on their analysis, the large mass flow rate through the chimney is one of the primary reasons for the energy losses. A numerical investigation of the dependence of the generated power on the collector and chimney geometry was performed by Koonsrisuk and Chitsomboon.[17] Their analysis revealed that a large increase in power output can be obtained through the combination of a sloping collector roof and a divergent chimney. The influence of the chimney geometry (such as area ratio between chimney inlet and outlet and divergence angle) on the power output was investigated numerically by Hu et al.[18] According to their study, divergent chimneys produce more power compared to the conventional cylindrical chimneys which supports the findings by Koonsrisuk and Chitsomboon.[17] Overall, most of the aforementioned publications are concerned with estimates of the generated power, calculations of the system efficiency, the comparison of different geometric configurations, the cost etc. None of these earlier studies accounted for the possibility of flow structures resulting from underlying instabilities. Very little is known about the hydrodynamic instability of the radial flow inside the collector of SCPPs. Instability can lead to coherent flow structures that will affect the performance of the collector. Publications concerned with the stability of radial RBP flows are very scarce. Van Santen et al.[19,20] carried out numerical simulations of a radial outward flow between two horizontal differentially heated circular plates with buoyancy-driven convection. Surprisingly, 3-D transverse rolls developed for very low Reynolds numbers (the Rayleigh number was above the critical value). This was a surprising finding since for the same conditions according to Gage and Reid[7] streamwise longitudinal vortex rolls are most unstable. Fasel et al.[21,22] carried out RANS calculations for different scales of the Manzanares SCPP and validated the cubic scaling law by Schlaich.[1] Large-eddy simulations by the same authors[21,22] for the collector of a 1:33 scale model of the Manzanares SCPP showed transverse rolls near the collector inlet and longitudinal rolls near the collector outlet which suggests the existence of RBP instability. The stability of the converging flow between two approximately parallel fixed disks was studied by Bernardes[23] and streamwise vortex rolls were discovered near the collector outflow when the Richardson number exceeded a critical value.

This paper reports on direct numerical simulations (DNS) of the inward radial flow inside a hypothetical SCPP collector. The focus is on both spatial buoyancy-driven and viscosity-driven instability. First, the Navier-Stokes code and the discretization are described. Three-dimensional DNS for a fixed subcritical Reynolds number and supercritical Rayleigh numbers were carried out for plane RBP flow, as well as radial and spiral buoyancy-driven flows. Fourier transforms of the simulation data provide the wavelengths, growth rates, amplitudes and phase distributions of the disturbance modes. The results are put in context by comparison with the neutral curves by Gage and Reid.[7]

II. Methodology

A. Governing Equations

The compressible Navier-Stokes equations in cylindrical coordinates can be written as a vector equation,[24]

$$\frac{\partial \mathbf{U}}{\partial t} + \frac{\partial \mathbf{A}}{\partial z} + \frac{\partial \mathbf{B}}{\partial r} + \frac{1}{r}\frac{\partial \mathbf{C}}{\partial \theta} + \frac{1}{r}\mathbf{D} = \mathbf{H}\,, \tag{4}$$

with state vector,

$$\mathbf{U} = \begin{bmatrix} \rho \\ \rho u \\ \rho v \\ \rho w \\ \rho e \end{bmatrix}, \tag{5}$$

and flux vectors,

$$\mathbf{A} = \begin{bmatrix} \rho u \\ \rho u^2 + p - \tau_{zz} \\ \rho u v - \tau_{rz} \\ \rho u w - \tau_{\theta z} \\ u(\rho e + p) - u\tau_{zz} - v\tau_{rz} - w\tau_{\theta z} + q_z \end{bmatrix}, \tag{6}$$

$$\mathbf{B} = \begin{bmatrix} \rho v \\ \rho v u - \tau_{rz} \\ \rho v^2 + p - \tau_{rr} \\ \rho v w - \tau_{\theta r} \\ v(\rho e + p) - u\tau_{rz} - v\tau_{rr} - w\tau_{\theta r} + q_r \end{bmatrix}, \tag{7}$$

$$\mathbf{C} = \begin{bmatrix} \rho w \\ \rho w u - \tau_{\theta z} \\ \rho w v - \tau_{\theta r} \\ \rho w^2 + p - \tau_{\theta\theta} \\ w(\rho e + p) - u\tau_{\theta z} - v\tau_{\theta r} - w\tau_{\theta\theta} + q_\theta \end{bmatrix}. \tag{8}$$

Here, u, v, and w are the velocities in the z (wall-normal), r (streamwise), and θ (azimuthal) direction, ρ is the density, and p is the static pressure. The total energy, $e = \epsilon + 1/2(u^2 + v^2 + w^2)$, is the sum of the internal energy, $\epsilon = c_v T$ and the kinetic energy. Here, c_v is the specific heat at constant volume, and T is the temperature. The source term vectors are

$$\mathbf{D} = \begin{bmatrix} \rho v \\ \rho u v - \tau_{rz} \\ \rho v^2 - \rho w^2 - \tau_{rr} + \tau_{\theta\theta} \\ 2\rho v w - 2\tau_{\theta r} \\ v(\rho e + p) - u\tau_{rz} - v\tau_{rr} - w\tau_{\theta r} + q_r \end{bmatrix}, \tag{9}$$

and

$$\mathbf{H} = \begin{bmatrix} 0 \\ g(\rho_{ref} - \rho) \\ 0 \\ 0 \\ ug(\rho_{ref} - \rho) \end{bmatrix}. \tag{10}$$

The vector $\mathbf{H}$ includes a buoyancy term that makes recourse to the Boussinesq approximation, $g(\rho_{ref} - \rho)$, with gravitational acceleration, $g = 9.81 m/s^2$. The shear stress tensor components are,

$$\tau_{zz} = \frac{2}{3}\mu\left[2\frac{\partial u}{\partial z} - \frac{\partial v}{\partial r} - \frac{1}{r}\left(\frac{\partial w}{\partial \theta} + v\right)\right], \tag{11}$$

$$\tau_{rr} = \frac{2}{3}\mu\left[-\frac{\partial u}{\partial z} + 2\frac{\partial v}{\partial r} - \frac{1}{r}\left(\frac{\partial w}{\partial \theta} + v\right)\right], \tag{12}$$

$$\tau_{\theta\theta} = \frac{2}{3}\mu\left[-\frac{\partial u}{\partial z} - \frac{\partial v}{\partial r} + 2\frac{1}{r}\left(\frac{\partial w}{\partial \theta} + v\right)\right], \tag{13}$$

and

$$\tau_{rz} = \mu\left[\frac{\partial u}{\partial r} + \frac{\partial v}{\partial z}\right], \tag{14}$$

$$\tau_{\theta z} = \mu\left[\frac{\partial w}{\partial z} + \frac{1}{r}\frac{\partial u}{\partial \theta}\right], \tag{15}$$

$$\tau_{\theta r} = \mu\left[\frac{1}{r}\left(\frac{\partial v}{\partial \theta} - w\right) + \frac{\partial w}{\partial r}\right], \tag{16}$$

with dynamic viscosity, μ. The heat flux vector components are,

$$q_z = -k\frac{\partial T}{\partial z}, \tag{17}$$

$$q_r = -k\frac{\partial T}{\partial r}, \tag{18}$$

$$q_\theta = -k\frac{1}{r}\frac{\partial T}{\partial \theta}, \tag{19}$$

with heat conduction coefficient, k. The set of equations is closed by the ideal gas equation,

$$p = \rho R T, \tag{20}$$

with gas constant, R, and Sutherland's law for the viscosity.

B. Non-Dimensionalization

The governing equations were made dimensionless with a reference velocity, v_{ref}, a reference length scale, L_{ref}, a reference temperature, T_{ref}, and a reference density, ρ_{ref}. Pressure was made dimensionless with $\rho_{ref} v_{ref}^2$. The Reynolds number based on maximum velocity and channel half-height is

$$Re = \frac{u_{max} \frac{h}{2}}{\nu}, \tag{21}$$

where h is the channel height. For the present simulations, the maximum velocity at the inflow was taken as reference velocity, v_{ref}, and the channel half-height was taken as reference length, $L_{ref} = h/2$. The Rayleigh number is defined as

$$Ra = \frac{\gamma h^3 g \Delta T}{\nu \alpha}, \tag{22}$$

where $\gamma = 1/T_{av}$ with $T_{av} = (T_{hot} + T_{cold})/2$ is the thermal expansion coefficient for a perfect gas, $\Delta T = T_{hot} - T_{cold}$, is the temperature difference between the bottom and top wall, and α is the thermal diffusivity. The Prandtl number is defined as

$$Pr = \frac{\nu}{\alpha}. \tag{23}$$

For the chosen reference quantities, the Rayleigh number can be written as

$$Ra = Re^2 \frac{\Delta T}{T_{av}} \left(\frac{h}{L_{ref}} \right)^3 \left(g \frac{L_{ref}}{v_{ref}^2} \right) Pr, \tag{24}$$

where gL_{ref}/v_{ref}^2 is the dimensionless gravitational acceleration. The reference Mach number was 0.1. In accordance with Gage and Reid,[7] the Prandtl number was set to one.

C. Computational Grid and Discretization

Pizza-slice shaped computational domains were employed for all simulations (Fig. 1). The inflow was at r_2 and the outflow was at $r_1 < r_2$. A coordinate transformation was employed in the wall-normal direction that clusters grid points near the walls. A total of J grid points were distributed in the wall-normal direction,

$$z_j = \left[\frac{\tan^{-1}(jc - f_1)}{f_2} + 1 \right] \times \frac{h}{2}, \tag{25}$$

where $h = 2$ is the channel height, $f_1 = Jc/2$ and $f_2 = \tan^{-1}(f_1)$, c is a user specified constant, and j is the grid line index. An equidistant grid point distribution was employed in the streamwise direction. The grid opening angle is an integer fraction of 2π.

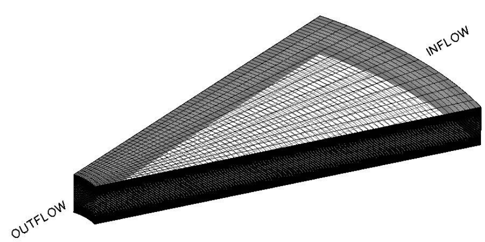

Figure 1. Computation grid for inward radial RBP flow simulation.

The convective terms in the wall-normal and radial direction were discretized with fifth-order-accurate upwind-biased,

$$\frac{1}{2} f'_{j-1} + f'_j + \frac{1}{6} f'_{j+1} \quad = \quad -\frac{1}{18} f_{j-2} - f_{j-1} + \frac{1}{2} f_j + \frac{5}{9} f_{j+1}, \tag{26}$$

and downwind-biased,

$$\frac{1}{2} f'_{j+1} + f'_j + \frac{1}{6} f'_{j-1} \quad = \quad \frac{1}{18} f_{j+2} + f_{j+1} - \frac{1}{2} f_j - \frac{5}{9} f_{j-1}, \tag{27}$$

compact finite differences.[25] The first and second derivatives of the viscous terms (wall-normal and radial direction) were discretized with fourth-order-accurate compact finite differences for non-equidistant meshes by Shukla et al.,[26]

$$a_{j-1}f^{(d)}_{j-1} + f^{(d)}_{j} + a_{j+1}f^{(d)}_{j+1} \quad = \quad b_{j-1}f_{j-1} + b_j f_j + b_{j+1}f_{j+1}\,. \tag{28}$$

Here d (either 1 or 2) represents the order of the derivative. The resulting tridiagonal systems of equations in the wall-normal and radial directions were solved with the Thomas algorithm. Derivatives in the periodic azimuthal (θ-coordinate) direction were calculated in Fourier space. The forward and backward Fourier transforms were computed with fast Fourier transforms. A fourth-order-accurate explicit low-storage Runge-Kutta method[27] was employed for time integration.

D. Boundary Conditions

In the azimuthal direction, periodic boundary conditions were implicitly enforced by the Fourier-based discretization. No-slip and no-penetration as well as isothermal boundary conditions were employed at both walls. The bottom, T_b, and top wall, T_t, temperature were held constant. When the viscous terms are neglected, the wall-normal pressure gradient at the walls depends only on the buoyancy term,

$$\frac{\partial p}{\partial z} = g(1-\rho)\,. \tag{29}$$

The $\partial p/\partial z$ derivative was computed with a fourth-order-accurate finite difference stencil. A non-reflecting boundary condition based on Riemann invariants[28] was employed at the inflow boundary. At the outflow boundary, a characteristics-based boundary condition by Gross and Fasel[29] was applied. Both boundary conditions require reference profiles. The reference profiles were obtained by solving the equations describing one-dimensional laminar RBP flow,

$$\frac{\partial p}{\partial x} = \mu \frac{\partial^2 u}{\partial y^2}\,, \tag{30}$$

$$\frac{\partial p}{\partial y} = (1-\rho)g\,, \tag{31}$$

$$k\frac{\partial^2 T}{\partial y^2} + \mu\left(\frac{\partial u}{\partial y}\right)^2 = 0\,, \tag{32}$$

with a shooting method.

E. Numerical Linear Stability Analysis

According to what is customary in linear stability theory (LST), a wave ansatz of the form

$$u'(r,z,\theta,t) = \sum \hat{u}(z)e^{i(\alpha r + \beta\theta - \omega t)}\,, \tag{33}$$

is made for the disturbances where $\alpha{=}\alpha_r{+}i\alpha_i$ is the streamwise (radial) wavenumber, β is the spanwise (azimutal) wavenumber, and $\omega{=}\omega_r{+}i\omega_i$ is the angular frequency. Here, $\hat{u}(z)$ are the eigenfunctions. For the present spatial simulations, $\omega_i = 0$. The real part of the streamwise, α_r, and the spanwise wavenumber, β, are related to the wavelengths via $\alpha_r = 2\pi/\lambda_r$ and $\beta = 2\pi/\lambda_\theta$. The real part of the angular frequency is related to the period via $\omega_r = 2\pi/T$. In this paper the modes are referenced by their temporal, n, and spanwise or azimuthal mode number, k. Spatial disturbance growth occurs for $\alpha_i < 0$.

The data obtained from the simulations were Fourier transformed in the azimuthal direction and in time. For example, the disturbance velocity at a given location is described by,

$$u'(r,z,\theta,t) = \hat{a}_{cc}(r,z)\cos\omega t\cos\beta r\theta + \hat{a}_{cs}(r,z)\cos\omega t\sin\beta r\theta + \hat{a}_{sc}(r,z)\sin\omega t\cos\beta r\theta + \hat{a}_{ss}(r,z)\sin\omega t\sin\beta r\theta\,. \tag{34}$$

The corresponding spanwise wavenumber and frequency are $\beta = 2\pi k/r\Theta$ and $\omega_r = 2\pi n/T$. The first subscript of the Fourier coefficients refers to time (cosine and sine mode). The second subscript refers to the azimuthal direction. From this, the amplitude and phase of the right traveling waves (in positive θ-direction, "+" superscript),

$$A = \sqrt{(\hat{a}_c^+)^2 + (\hat{a}_s^+)^2}\,, \tag{35}$$

and

$$\psi = -\tan^{-1}\frac{\hat{a}_s^+}{\hat{a}_c^+}\,, \tag{36}$$

can be obtained, where $\hat{a}_c^+ = (\hat{a}_{cc} + \hat{a}_{ss})/2$ and $\hat{a}_s^+ = (\hat{a}_{cs} - \hat{a}_{sc})/2$. Analogously, for the left traveling waves (in negative θ-direction, "-" superscript),

$$A = \sqrt{(\hat{a}_c^-)^2 + (\hat{a}_s^-)^2}\,, \tag{37}$$

and

$$\psi = -\tan^{-1}\frac{\hat{a}_s^-}{\hat{a}_c^-}\,, \tag{38}$$

can be derived with $\hat{a}_c^- = (\hat{a}_{cc} - \hat{a}_{ss})/2$ and $\hat{a}_s^- = -(\hat{a}_{cs} + \hat{a}_{sc})/2$. The spatial growth rates can be computed from

$$\alpha_i = -\frac{\partial \ln A}{\partial s}\,, \tag{39}$$

where s is the arclength in the radial direction measured from the inflow,

$$s = r_2 - r\,. \tag{40}$$

Because of $\psi = \alpha_r r + \beta r\theta - \omega_r t$, the phase speed in the radial direction is

$$c_r = -\frac{\frac{\partial\psi}{\partial t}}{\frac{\partial\psi}{\partial x}} = \frac{\omega_r}{\alpha_r} \tag{41}$$

and the phase speed in the wave propagation direction is

$$c = \frac{\omega_r}{K}\,, \tag{42}$$

where $K = \sqrt{\alpha_r^2 + \beta^2}$.

F. Parameters for Different Cases

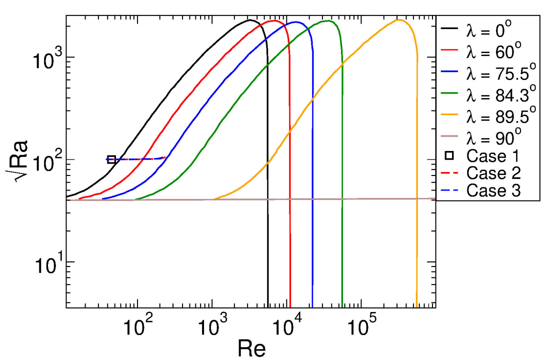

Figure 2. Investigated cases (lines) plotted in stability diagram by Gage and Reid.[7] Case 4 and case 6 are not shown.

The present stability simulations were set up according to the neutral curves by Gage and Reid[7] (Fig. 2). A total of six cases (Tab. 1) were investigated. The cases were chosen such that the flow is unstable either (1) with respect to 3-D (longitudinal) waves or (2) with respect to 2-D transverse waves. Since the flow is accelerating in the radial direction, the Reynolds and Rayleigh number for cases 2 and 3 follow lines in Fig. 2.

	Re	$\sqrt{Ra}$	Inflow radius (r_2)	Outflow radius (r_1)	Instability
case 1	45	100	$40 + 10^7$	10^7	Buoyancy-driven (Plane RBP)
case 2	45	100	22.918	3	Buoyancy-driven (Radial RBP)
case 3	45	100	22.918	3	Buoyancy-driven (Spiral RBP)
case 4	10000	0	$35 + 10^7$	10^7	Viscosity-driven ($T_b = T_t$, Plane RBP)

Table 1. Parameters for spatial stability simulations. ***Re*** **is reference inflow Reynolds number.**

III. Results

Since the radial velocity exhibits a hyperbolic dependence on the radius, the flow is strongly accelerated. Acceleration is known to be stabilizing[10] and also leads to non-parallel effects (that were not considered by Gage and Reid[7]). Therefore, the stability of inward radial RBP flow is expected to be different from the stability of plane RBP flow. Earlier radial RBP flow simulations by Kamrul and Gross[30] showed that the stability was markedly different near the chimney entrance (collector exit).

A. Buoyancy-Driven Instability

1. Plane RBP Flow

For the first spatial simulation (case 1), the inflow radius was set to $r_2 = 40 + 10^7$ and the outflow radius was set to $r_1 = 10^7$. The azimuthal grid extent was $r_2\Theta = 6$. Because of the very large inflow and outflow radius,

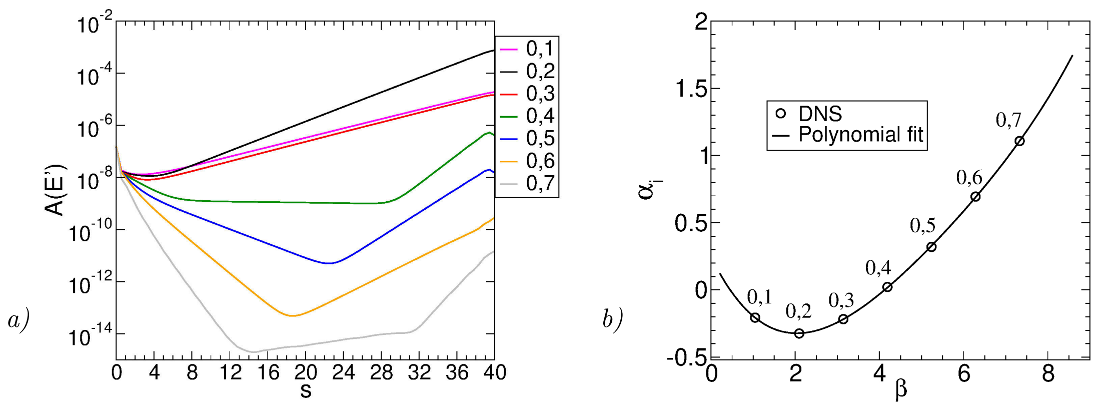

Figure 3. ***a)*** **Azimuthal Fourier modes of disturbance kinetic energy vs. streamwise arclength and** ***b)*** **growth rates vs. azimuthal wavenumber and polynomial curve fit at** ***s*****=10 for case 1.**

this simulation effectively models a plane channel flow. The bottom and top wall temperatures were set to $T_b = 350K$ & $T_t = 300K$. Randomized steady velocity disturbances with a maximum amplitude of 10^{-6} were introduced at the inflow boundary. Since $Re = 45 < Re_c$ and $\sqrt{Ra} = 100 > \sqrt{Ra}_c$, 3-D disturbances are expected to grow according to Gage and Reid.[7] The azimuthal wavelength of the modes was computed as,

$$\lambda_\theta = \frac{r\Theta}{k} = \frac{(r_2 - s)\Theta}{k}\,, \tag{43}$$

The azimuthal mode amplitudes were computed from the integrated (across the height) disturbance kinetic energy and are shown in Fig. 3a. Slight discontinuities near the inflow and outflow boundaries can be attributed to the boundary conditions. Mode (0,2), which has an azimuthal wavelength of $\lambda_\theta = 3$, exhibits the strongest linear growth. Modes (0,1) and (0,3) also grow linearly. The other modes initially decay and then exhibit secondary growth once the primary modes reach sufficiently large nonlinear amplitudes. In Fig. 3b the growth rate is plotted versus the azimuthal wavenumber for $s = 10$. For this downstream location all modes exhibit primary linear growth or decay. Mode (0,2) with azimuthal wavenumber $\beta = 2.094$ experiences the strongest growth with $\alpha_i = -0.3238$.

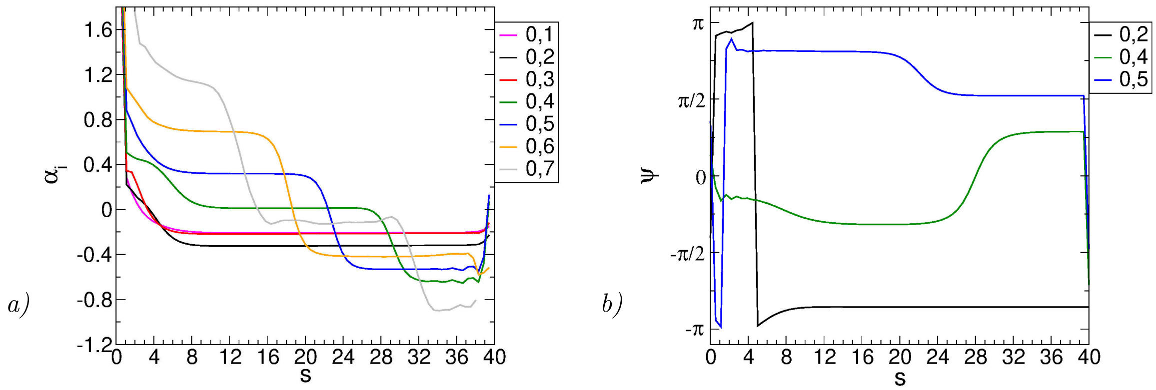

Figure 4. ***a)*** **Growth rates and** ***b)*** **azimuthal phases vs. streamwise arclength for case 1.**

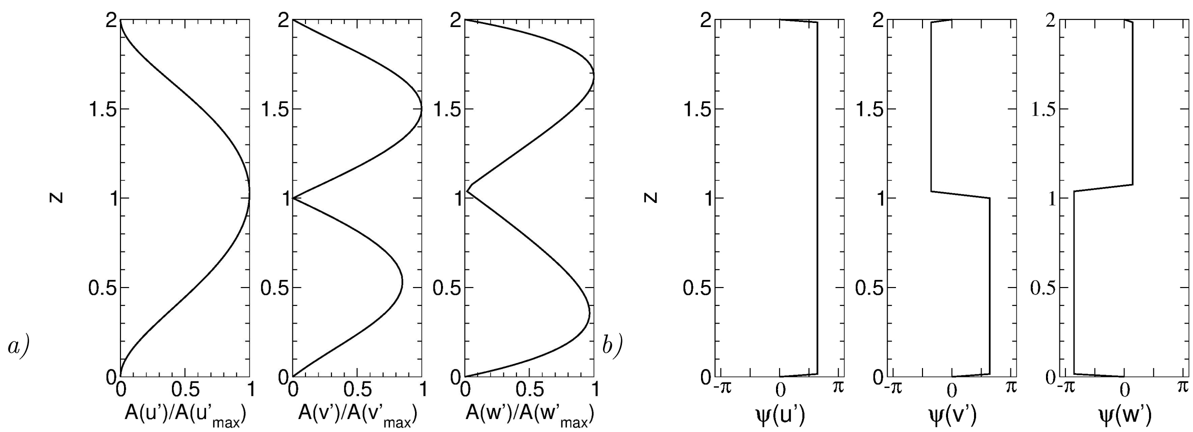

Figure 5. ***a)*** **Mode shapes and** ***b)*** **phase distribution for mode (0,2) at** $s = 30$ **for case 1.**

Interactions among waves are possible in the DNS and modes can exhibit secondary growth due to non-linear effects or resonances. In Fig. 4a the growth rates are plotted over the streamwise distance. Mode (0,7) is the first to experience secondary growth. Later on and further downstream, modes (0,6)-(0,4) also experience secondary growth. Interestingly, mode (0,6) starts to show non-linear growth at $s \approx 17$ where the growth of mode (0,7) becomes constant. Similar observations can be made for modes (0,6) and (0,5) half way through the channel and for modes (0,5) and (0,4) further downstream. The spatial development of the azimuthal phase is plotted in Fig. 4b. Changes of the growth rates go hand-in-hand with phase adjustments. For instance, the suddenly increased growth rate of mode (0,4) for $s > 28$ can be associated with a phase alignment of mode (0,4) that likely results in a non-linear energy transfer from mode (0,2) to mode (0,4) due to resonance.

The amplitude and phase distributions of the disturbance velocity for the primary mode (0,2) at $s = 30$ are provided in Fig. 5a and Fig. 5b respectively. The radial (v') and azimuthal (w') amplitude distributions for the primary mode $(0, 2)$ have two peaks near $z \approx 1.5$ and a phase-jump of π at $z = 1$. The wall-normal u' disturbance amplitude exhibits only one peak at the mid-channel height and a constant phase distribution away from the walls.

The present spatial stability results (case 1) obtained with the new radial code are in agreement with earlier temporal stability simulations by Kamrul and Gross.[31] According to Kamrul and Gross,[31] $\lambda_\theta = 3$ has the highest temporal growth rate. A comparison of the growth rates with the temporal simulations would be desirable. However, since the modes are steady ($\omega_r = 0$), the phase speed $c = \omega_r/\sqrt{\alpha_r^2 + \beta^2}$ is zero and the Gaster transform cannot be invoked to make a connection between the temporal and spatial growth rates.

2. Radial Flow

The inflow Reynolds and Rayleigh number for case 2 were the same as for case 1. The inflow and outflow radius were set to $r_2 = 22.918$ and $r_1 = 3$. The grid openig angle was 30 degree. The bottom and top wall temperature were set to $T_b = 350K$ & $T_t = 300K$. Figure 6a shows streamlines computed from the velocities at the channel half height. In this and many of the following figures the computational domain was repeated in the circumferential direction to show the entire collector. The local Reynolds number based on the maximum radial velocity is plotted in Fig. 6b. An almost hyperbolic increase of the Reynolds number (radial velocity) is observed. This is in agreement with the continuity equation which predicts $\rho v \propto 1/r$. The Reynolds number at the outflow is approximately 240. A DNS with 8 azimuthal Fourier modes was carried out. Randomized steady velocity disturbances with a maximum amplitude of 10^{-6} were introduced at the inflow boundary. Steady azimuthal Fourier modes of the disturbance kinetic energy are plotted in Fig. 7. Mode (0,6) has the largest amplitude for $s < 8.5$ after which mode (0,5) attains the maximum amplitude. Towards the outflow mode (0,2) dominates. This suggests that as the flow approaches the collector outflow, the higher modes are less amplified or even damped while the lower modes are more amplified. Because the wavelength has to be an integer fraction of the circumference, only certain wavelengths are possible. For an observer, the vanishing of mode (0,6) and emergence of modes (0,5) & (0,2) have the appearance of a "vortex merging".

a)

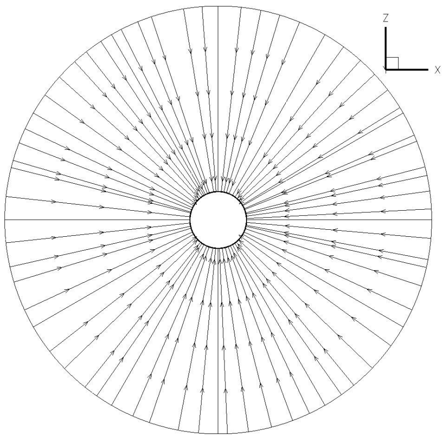

b)

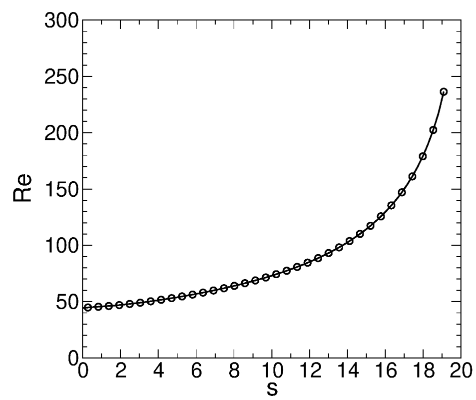

Figure 6. ***a)*** **Streamlines and** ***b)*** **local Reynolds number vs. streamwise arclength for case 2.**

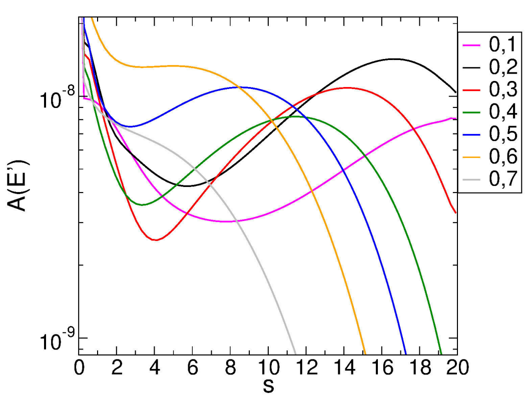

Figure 7. Azimuthal Fourier modes of disturbance kinetic energy vs. streamwise arclength for case 2.

In Fig. 8a the growth rates are plotted over the streamwise arclength. The discontinuities of the growth rates near the inflow and outflow boundaries can be attributed to the boundary conditions. Also, the disturbances introduced at the inflow may not exactly satisfy the governing equations. Finally, receptivity which is not adressed in this paper, likely affects the mode amplitudes near the inflow. Different from

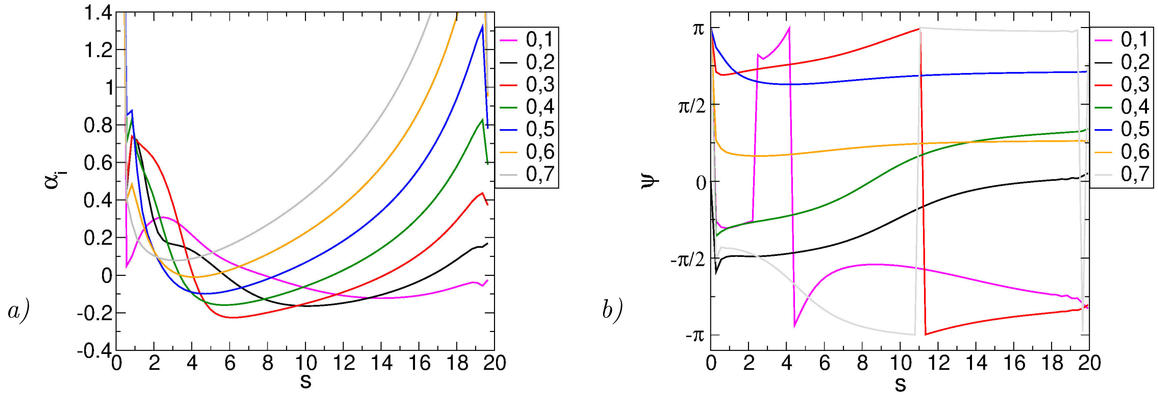

Figure 8. ***a)*** **Spatial growth rate and** ***b)*** **azimuthal phases vs. streamwise arclength for case 2.**

case 1, because the basic flow is accelerating in the streamwise direction, the growth rates are constantly changing. Near the inflow, mode (0,5) is the most amplified. Mode (0,3) experiences maximum growth (most negative α_i) between $s \approx 4.7$ and $s \approx 9.5$. For $9.5 < s < 13.5$, mode (0,2) and for $s > 13.5$ mode (0,1) are strongly amplified (lower mode numbers are more strongly amplified downstream). For $s > 13.5$ the azimuthal wavelength of mode (0,1) is between $\lambda_\theta = 4.93$ and $\lambda_\theta = 1.57$. In agreement with the earlier plane RBP flow stability simulation (case 1), the azimuthal wavelength of the wave that experiences the strongest amplification is approximately three. Because the azimuthal, $r\Theta$, extent changes with r, the mode number is adjusting in r. The growth rates of the unstable modes for case 2 never reach the growth rate of the most unstable mode ($\lambda_\theta = 3$) for case 1. This may be attributed to the strong acceleration (hyperbolic increase of Reynolds number in the radial direction) which is known to be stabilizing.

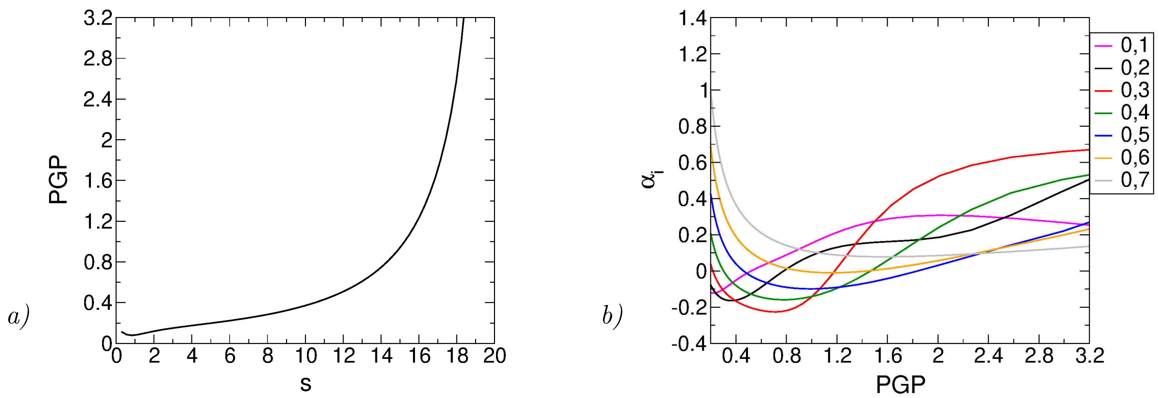

Figure 9. ***a)*** **Pressure gradient parameter vs. streamwise arclength and** ***b)*** **growth rate of steady modes vs. pressure gradient parameter for case 2.**

The phase distribution computed from the azimuthal velocity component are plotted in Fig. 8b. The changes in growth rate can be correlated with phase adjustments. Different from case 1, the phase adjustments are more gradual. For example, the increased growth of mode (0,2) for $6 < s < 17$ and mode (0,3) for $4 < s < 15$ and the following reduction of the growth rates (Fig. 8a) can be associated with phase shifts (Fig. 8b). Similar observations can also be made for mode (0,4). The azimuthal phase of modes (0,5) and (0,6) are almost constant over the entire radial extent of the domain.

The dimensionless pressure gradient parameter, $PGP = (\theta^2/\nu) \times (dv_{max}/dx)$ is frequently invoked when the effect of pressure gradients on boundary layer stability is investigated. Assuming a parabolic velocity profile, the momentum thickness is $\vartheta = 2h/15$. Since this is a constant, it is omitted here. When furthermore $\nu = \nu_{ref}$ is assumed, the PGP simplifies to $PGP = Re \times (dv_{max}/dx)$. In Fig. 9a the pressure gradient parameter is plotted over the streamwise arclength. Because of the hyperbolic nature of the radial velocity, the PGP increases strongly in the radial direction. In Fig. 9b the growth rates are plotted versus the pressure gradient parameter. The growth rates of the steady azimuthal modes decrease as the PGP increases. The Plane RBP flow results are approached as the PGP approaches zero.

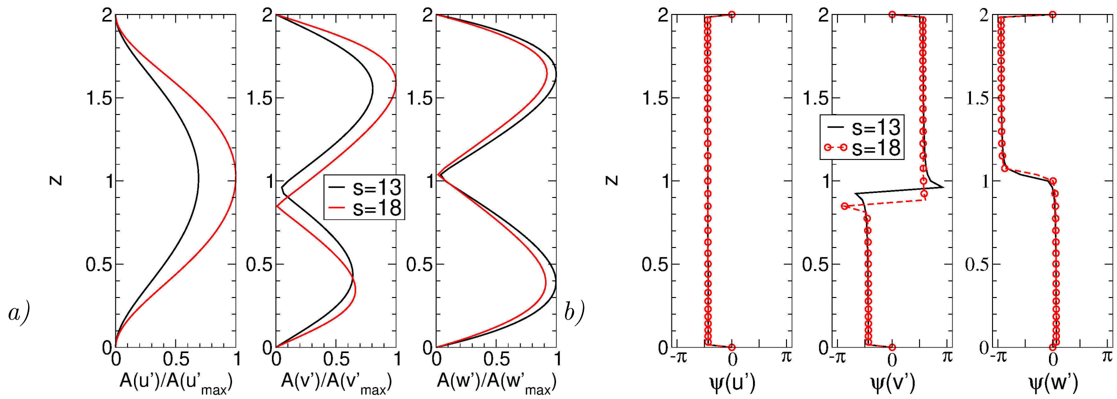

Figure 10. *a)* Mode shapes and *b)* phase distributions for mode (0,2) at $s = 13$ and $s = 18$ for case 2.

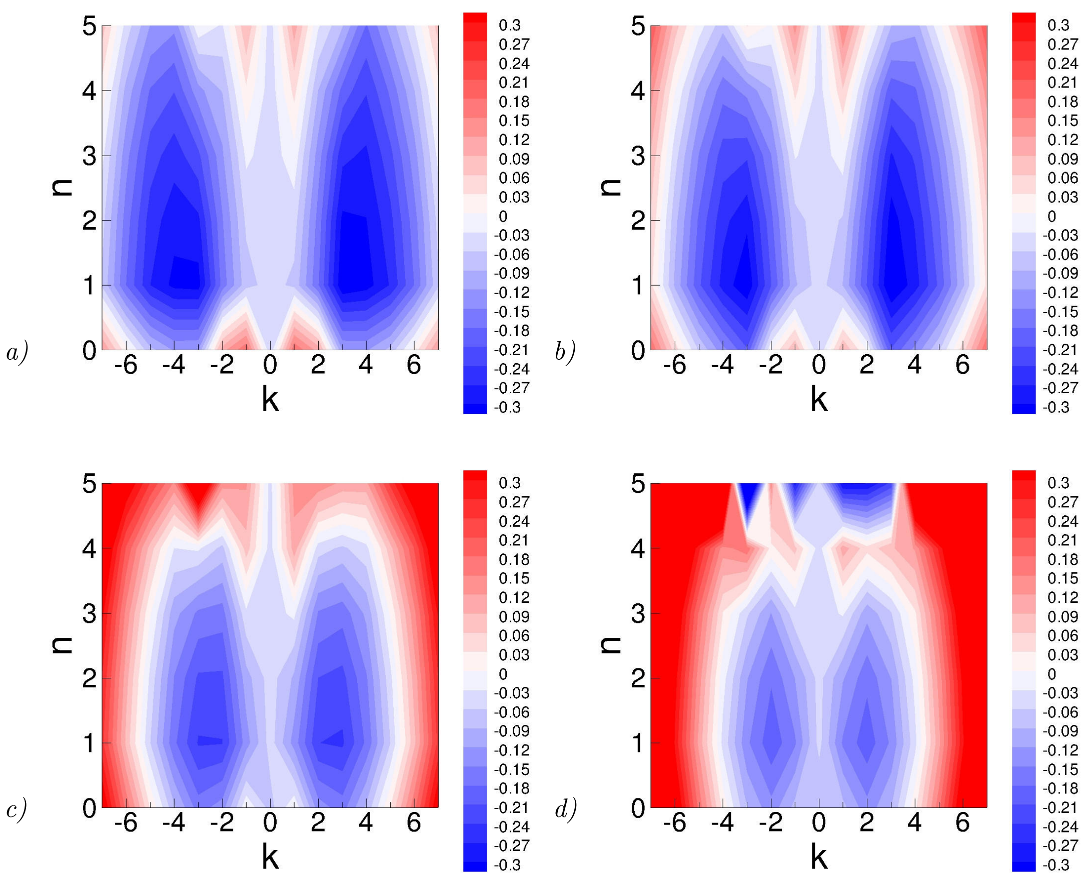

Figure 11. Spatial growth rate as a function of temporal and azimuthal mode number for *a)* $s = 4.7$, *b)* $s = 6.08$, *b)* $s = 8.85$ and *d)* $s = 11.6$ (case 2).

The amplitude and phase distributions of the wall-normal (u'), radial (v') and azimuthal (w') disturbance velocities for mode (0,2) at two different radial locations ($s = 13$ and $s = 18$) are shown in Fig. 10. The u'

amplitude distributions have only one peak near the channel mid-height and a constant phase over most of the channel height. In contrast, the v' and w' amplitude distributions have two peaks and a phase-jump of π at $z \approx 1$.

According to Gage and Reid,[7] below the critical Reynolds number for the T-S instability, oblique waves in plane RBP flow can be amplified if the Rayleigh number is large enough. It is therefore very interesting to see whether the oblique modes are also amplified in radial RBP flow. To this end, all three disturbance velocity components were Fourier transformed in time and then Fourier transformed in the azimuthal direction. This allows for an extraction of the amplitude and phase of the oblique Fourier modes for different frequencies as explained in section II.E. The total non-dimensional simulation time was $T = 60$ which sets the lowest frequency, $\omega_r = 0.1047$. In Fig. 11 contours of the spatial growth rate are plotted versus the temporal and azimuthal mode number for four streamwise locations. The growth rates of the strongest growing left and right traveling waves are identical. The highest growth rate is obtained for the smallest temporal mode number which corresponds to the lowest resolved frequency, $\omega_r = 0.1047$. This may be an artefact of the post-processing of the data and will be further investigated. Closer to the outflow, lower azimuthal mode numbers ($\pm k$) become dominant and the growth rates decrease.

a) *b)* *c)*

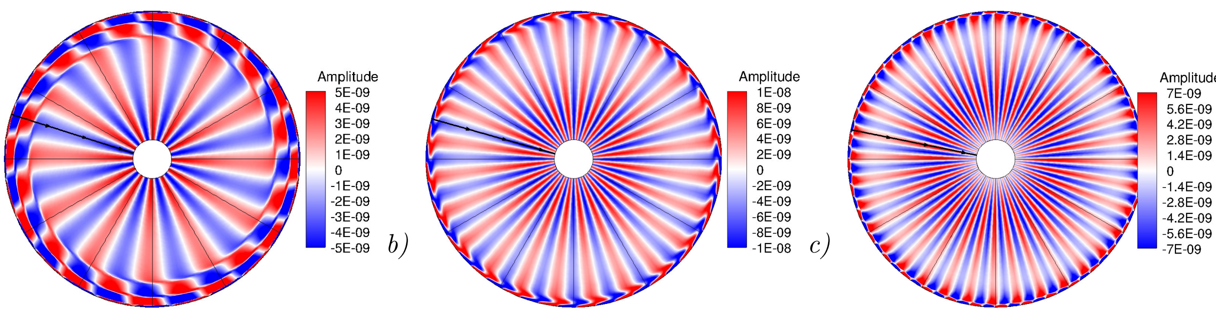

Figure 12. Disturbance kinetic energy for $\omega_r = 0$: *a)* $k = 1$, *b)* $k = 2$ and *c)* $k = 3$ for case 2.

The mode shapes were reconstructed from the amplitude and phase distributions. The mode shapes for $k = 1$, $k = 2$ & $k = 3$ and $\omega_r = 0$ (steady modes) have wave fronts that are aligned in the radial direction (Fig. 12). As a reference, streamlines at the channel half-height were included in the figures. Figures 13 and 14 illustrates the left and right traveling waves for $k = 1$, $k = 2$ & $k = 3$ for $\omega_r = 0.1047$ and $\omega_r = 0.3141$, respectively. The left and right traveling oblique modes are symmetric with respect to the streamlines. The wave angle decreases in the streamwise direction.

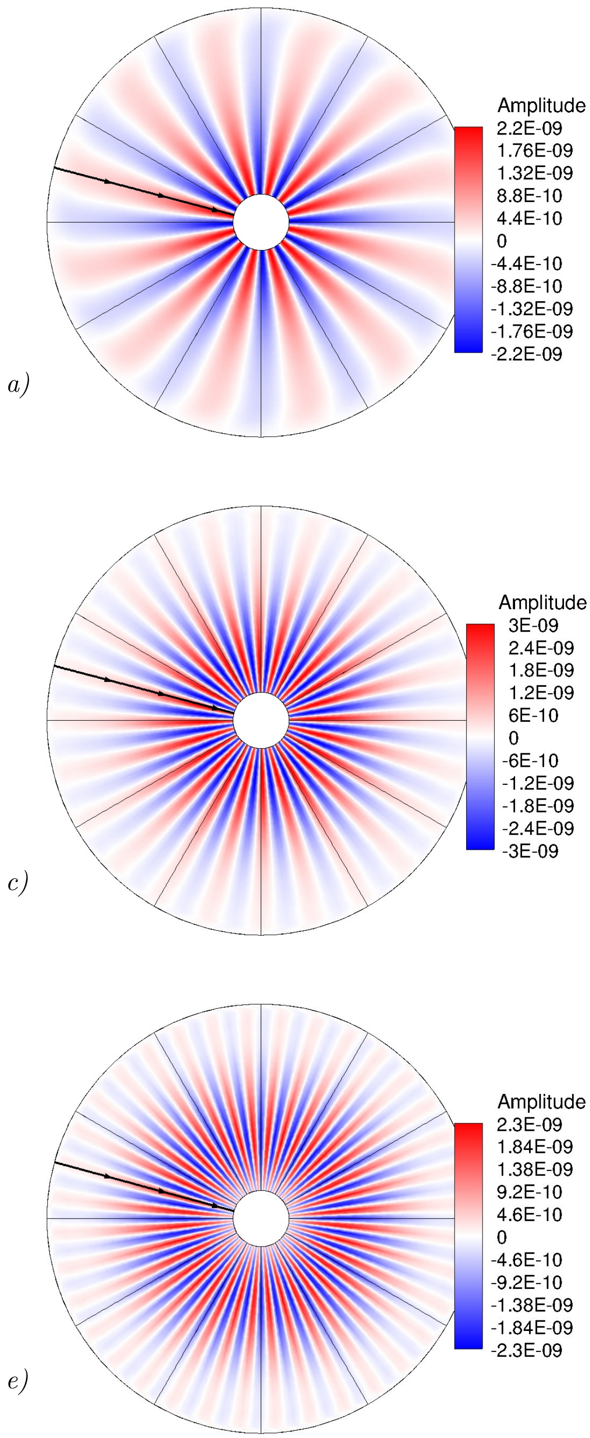

Figure 13. Disturbance kinetic energy for $\omega_r = 0.1047$: *a)* left traveling wave ($k = 1$), *b)* right traveling wave ($k = 1$), *c)* left traveling wave ($k = 2$), *d)* right traveling wave ($k = 2$), *e)* left traveling wave ($k = 3$) and *f)* right traveling wave ($k = 3$) for case 2.

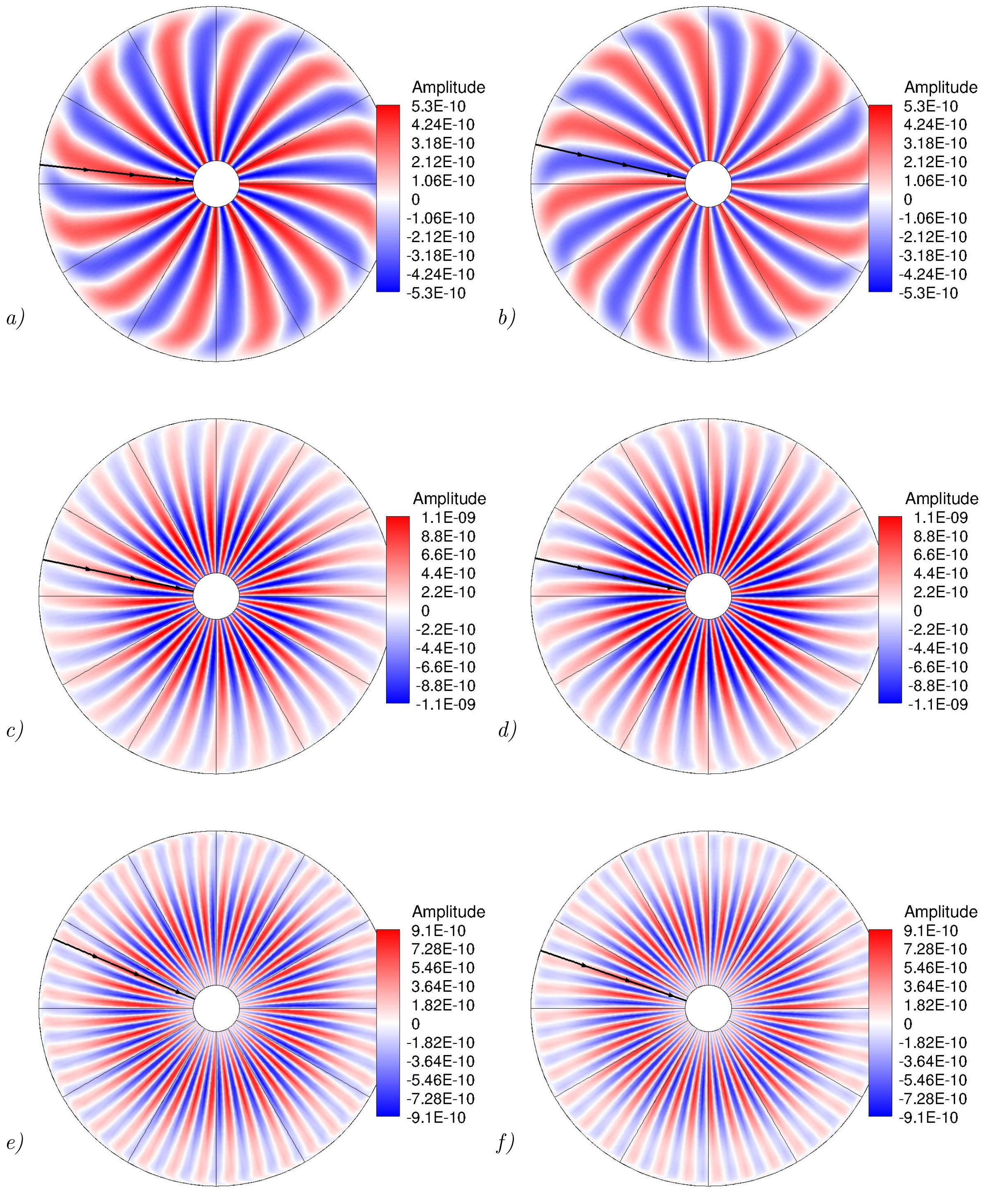

Figure 14. Disturbance kinetic energy for $\omega_r = 0.3141$: *a)* left traveling wave ($k = 1$), *b)* right traveling wave ($k = 1$), *c)* left traveling wave ($k = 2$), *d)* right traveling wave ($k = 2$), *e)* left traveling wave ($k = 3$) and *f)* right traveling wave ($k = 3$) for case 2.

3. Spiral Flow

Case 3 is identical to case 2 with the one difference that the inflow angle was set to 45 deg. Figure 15a illustrates the spiral streamlines resulting from the inclined inflow. As for case 2, the local Reynolds number for case 3 increases hyperbolically in the streamwise direction as seen in Fig. 15b. The maximum absolute radial and azimuthal velocity are plotted in Fig. 16a. Neglecting the viscous terms in the θ-momentum equation, one obtains

$$\frac{\partial(\rho v w)}{\partial r} + \frac{1}{r}(2\rho v w) = 0. \tag{44}$$

This suggests

$$w \propto \frac{1}{\rho v}\frac{1}{r^2} = r\frac{1}{r^2} = \frac{1}{r}. \tag{45}$$

Interestingly, in the simulation the w-velocity drops initially and then begins to grow hyperbolically (Fig. 16a). Because of the initial drop of the azimuthal velocity, the flow angle, $\phi = tan^{-1}(w/|v|)$ decreases considerably in the streamwise direction (Fig. 16b). The fact that the inflow angle is less than 45 deg, can be attributed to the inflow boundary condition which does not precisely hold the desired inflow value.

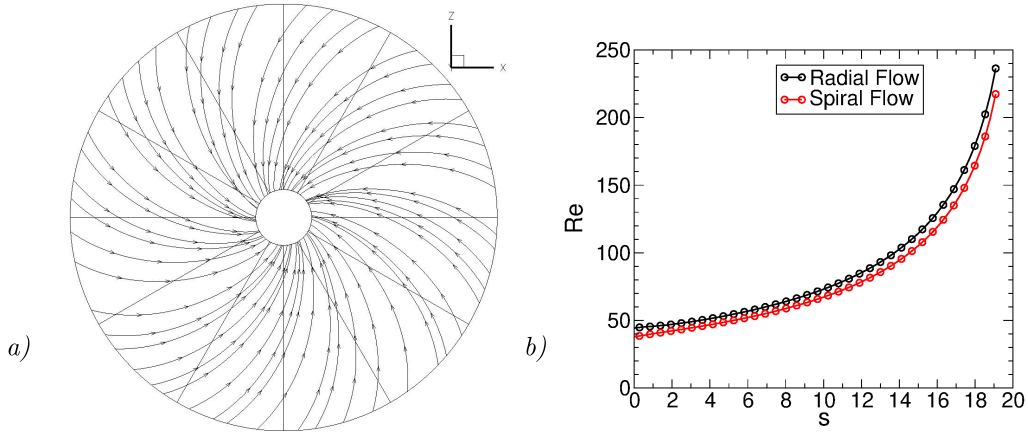

Figure 15. *a)* Streamlines for spiral flow simulation and *b)* local Reynolds number vs. streamwise arclength.

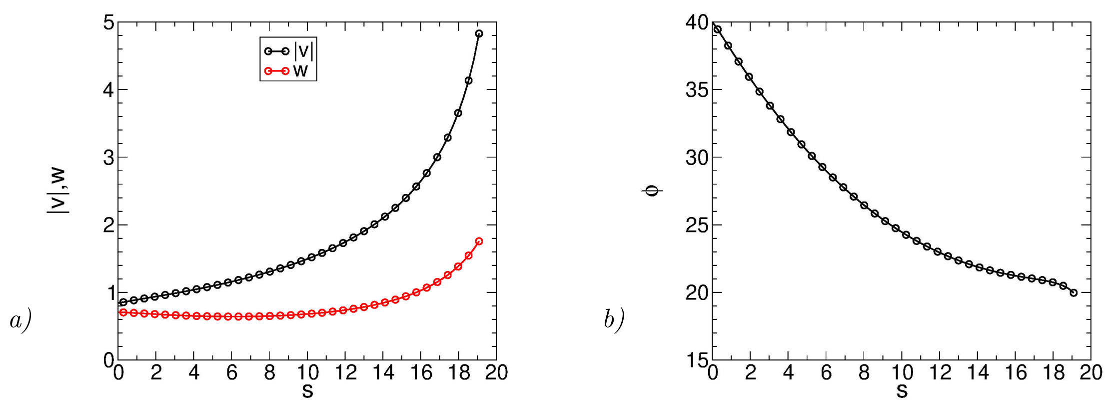

Figure 16. *a)* Radial (absolute) & azimuthal velocity and *b)* flow angle vs. streamwise arclength for case 3.

Similar to case 2, a simulation with 8 azimuthal Fourier modes was carried out. The steady azimuthal Fourier mode amplitudes computed from the disturbance kinetic energy are plotted in Fig. 17a. As for the radial flow (case 2), the mode number of the most unstable mode decreases in the streamwise direction. The growth rates are plotted in Fig. 17b. Included are the results for the radial flow. Figure 17b reveals that the growth rates of the steady modes for the spiral flow (case 3) are lower than for the radial flow (case 2).

Near the inflow, (0,3) is the most amplified. Between $s \approx 6$ and $s \approx 11.5$ mode (0,2) experiences maximum amplification. For $s > 11.5$ mode (0,1) is the strongest (lower mode numbers are more strongly amplified downstream).

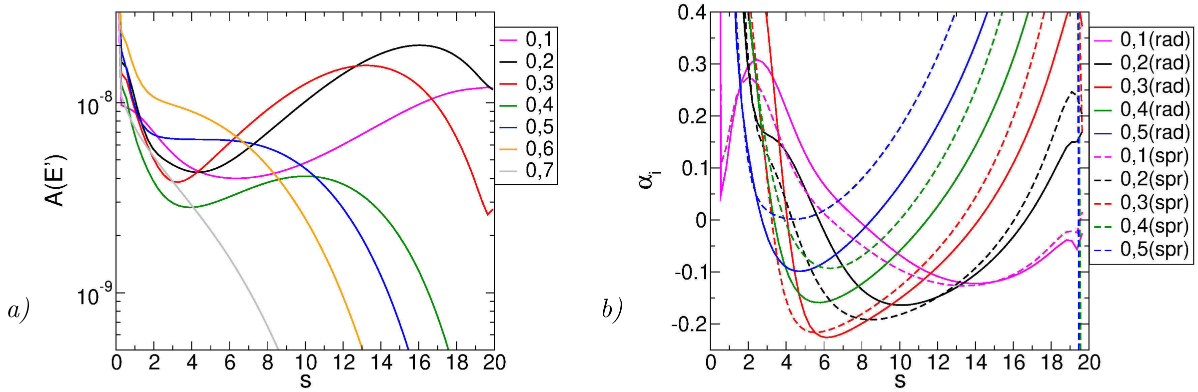

Figure 17. ***a)*** **Spatial evoluton of azimuthal Fourier modes of disturbance kinetic energy (spiral flow) and** ***b)*** **growth rates vs. streamwise arclength for case 3 (rad=radial, spr=spiral).**

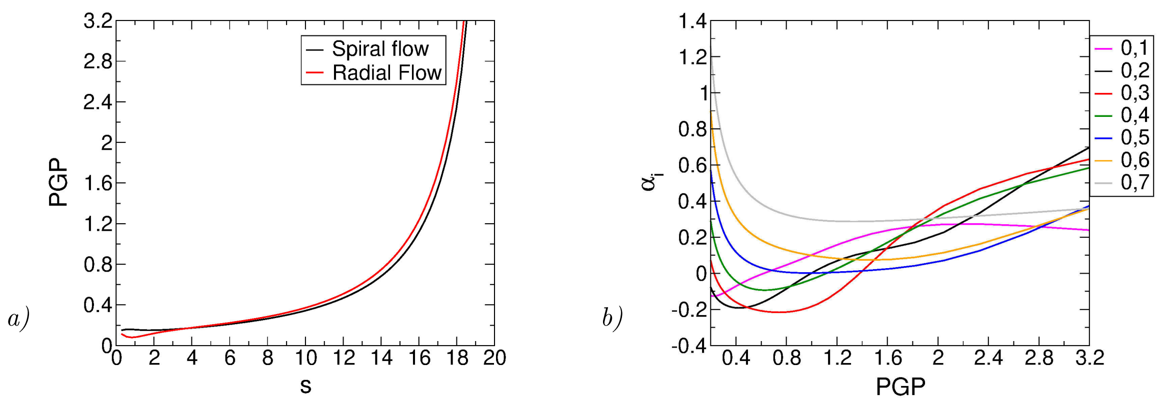

Figure 18. ***a)*** **pressure gradient parameter vs. streamwise arclength and** ***b)*** **growth rate of steady modes vs. pressure gradient paramet for case 3.**

In Fig. 18a the PGP is plotted over the streamwise arclength for both the radial and spiral flow. The PGP is marginally higher for the radial flow than for the spiral flow. Interestingly, different from the radial flow, for the spiral flow some modes remain amplified up to a larger PGP. For example, mode (0,3) is amplified for $0.2 < PGP < 1.2$ for the radial flow (Fig. 9b) and $0.2 < PGP < 1.4$ for the spiral flow (Fig. 18b).

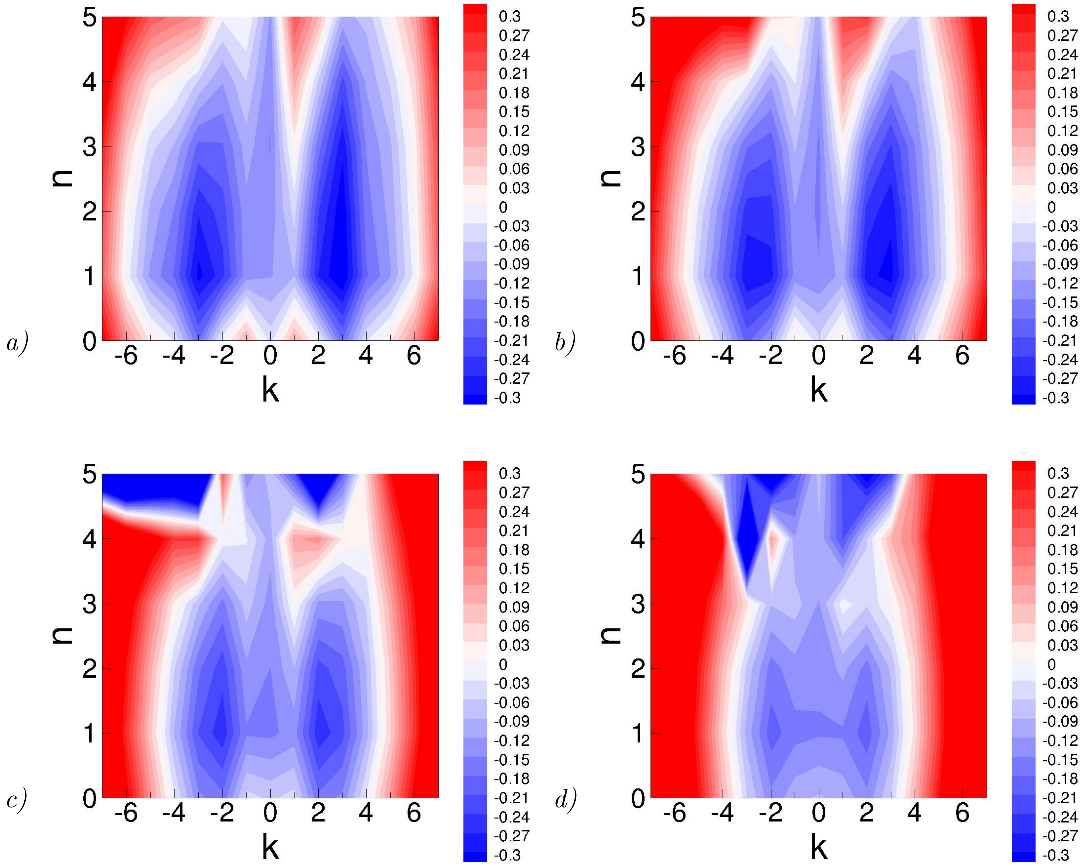

Figure 19. Spatial growth rate as a function of temporal and azimuthal mode number for *a)* $s = 4.7$, *b)* $s = 6.08$, *b)* $s = 8.85$ and *d)* $s = 11.6$ (case 3).

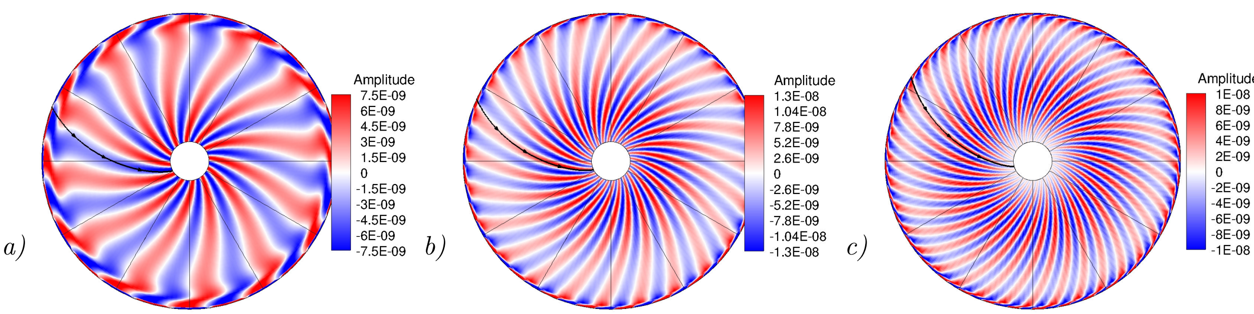

Figure 20. Disturbance kinetic energy for $\omega_r = 0$: *a)* $k = 1$, *b)* $k = 2$ and *b)* $k = 3$ for case 3.

Iso-contours of the spatial growth rates for four streamwise locations are plotted in Fig. 19. Surprisingly, the growth rates of the strongest growing left and right traveling modes are different meaning that one family of oblique modes is favored. Visualizations of the mode shapes for $\omega_r = 0$ (steady modes) are shown in Fig. 20. The wave fronts of the steady modes are spiral and tangential to the streamlines. The oblique modes for $\omega_r = 0.1047$ and $\omega_r = 0.3141$ are shown in Figs. 21 and 22. Different from the radial flow, the angle of the left and right traveling modes with respect to the streamlines is different. Because of the larger amplification, the left traveling oblique modes reach higher amplitudes than the right traveling oblique waves.

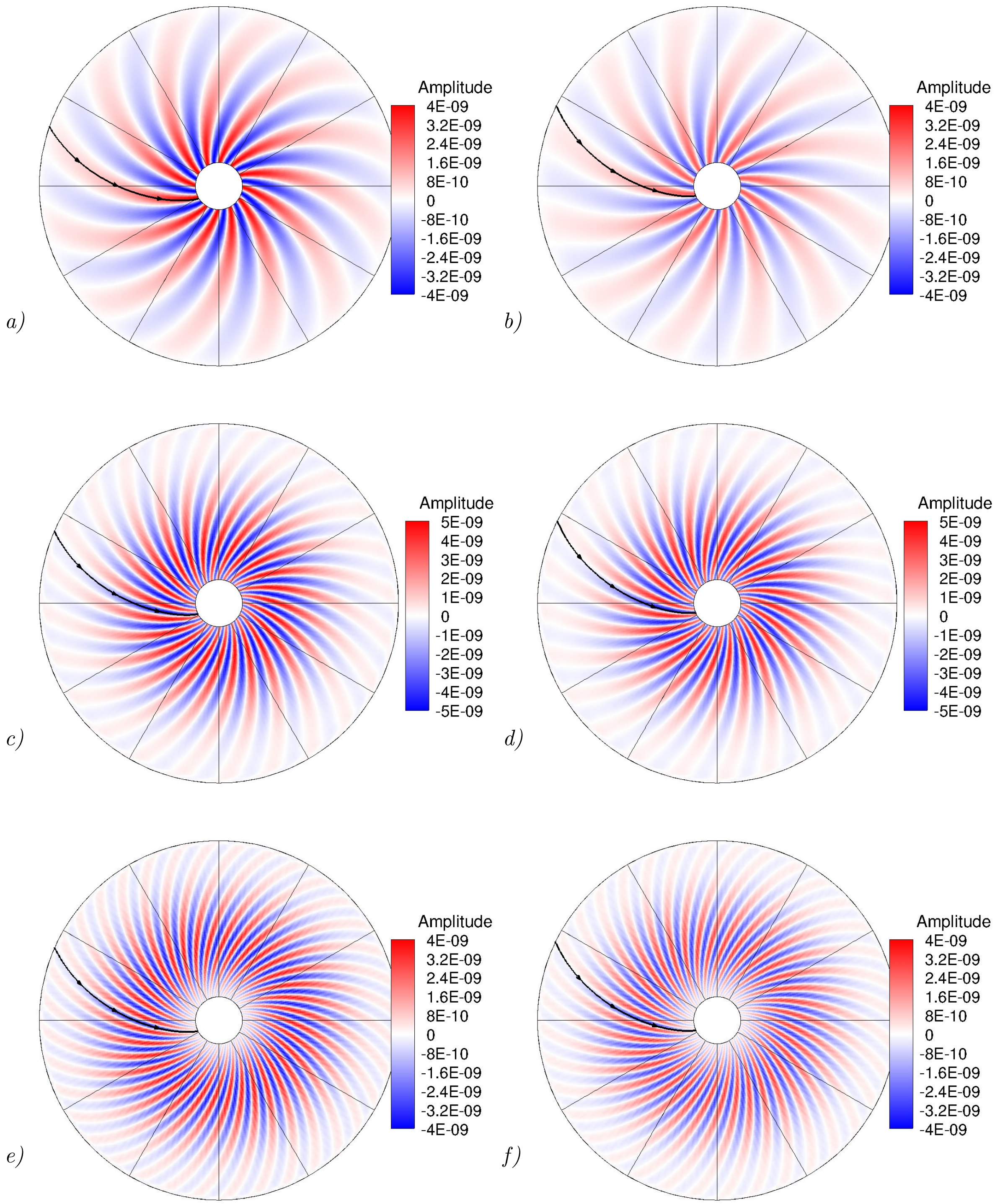

Figure 21. Disturbance kinetic energy for $\omega_r = 0.1047$: *a)* left traveling wave ($k = 1$), *b)* right traveling wave ($k = 1$), *c)* left traveling wave ($k = 2$), *d)* right traveling wave ($k = 2$), *e)* left traveling wave ($k = 3$), *f)* right traveling wave ($k = 3$) for case 3.

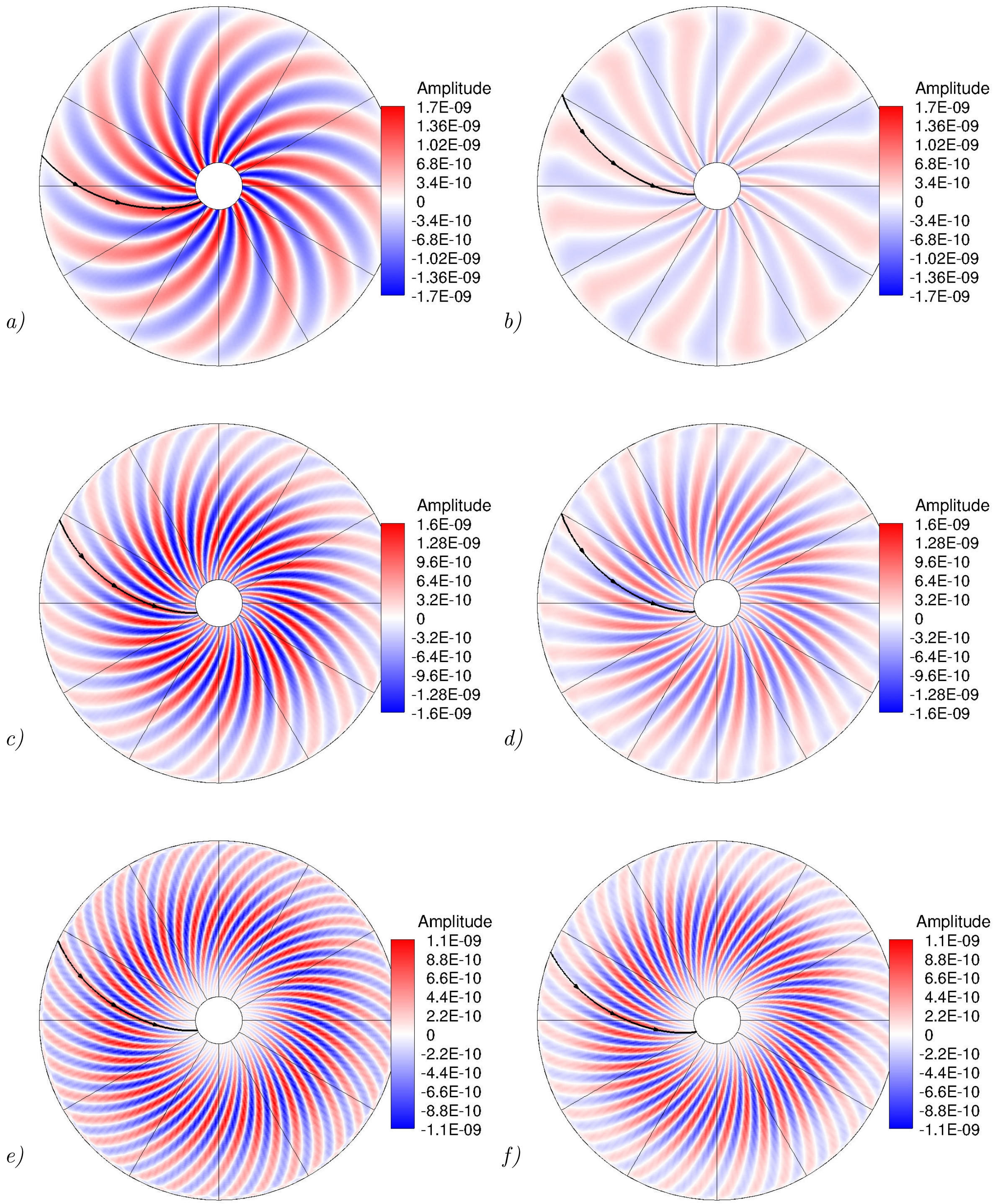

Figure 22. Disturbance kinetic energy for $\omega_r = 0.3141$: *a)* left traveling wave ($k = 1$), *b)* right traveling wave ($k = 1$), *c)* left traveling wave ($k = 2$), *d)* right traveling wave ($k = 2$), *e)* left traveling wave ($k = 3$), *f)* right traveling wave ($k = 3$) for case 3.

B. Viscosity-Driven Instability

The hydrodynamic instability of a plane Poiseuille flow (no heated walls, no gravitational field) was also investigated for a validation case from the literature. A case by Chung et al.[32] with a Reynolds number of $Re = 10,000$ based on maximum velocity and channel half-height was considered. According to Chung et al.,[32] an unstable mode exists with $\alpha = 1.0006 - i0.0109$ and $\omega_r = 0.23753$. For this simulation (case 4) the inflow radius was $r_2 = 35 + 10^7$ and the outflow radius was $r_1 = 10^7$. The bottom and top wall temperature were set to $T_b = T_t = 300K$ and different from the other cases, the Prandtl number was $Pr = 0.71$. Since $Re = 10,000 > Re_c$ and $\sqrt{Ra} < \sqrt{Ra_c}$, 2-D disturbances are expected to grow according to Gage and Reid.[7] The linear disturbance mode was extracted from a precursor simulation with matching parameters. The mode was rescaled to a maximum amplitude of 4×10^{-5} and introduced at the inflow boundary of the spatial simulation. The inflow disturbance frequency was set to 0.23753 according to Chung et al.[32] The mode amplitude and growth rate obtained from the simulation are shown in Fig. 23. In agreement with Gage and Reid[7] and Chung et al.,[32] linear growth (Tollmien-Schlichting instability) is observed for case 4 (Fig. 23a) as the combination of $Re - \sqrt{Ra}$ is above the $\lambda = 0$ degree neutral curve in Fig. 2. The disturbance amplitude experiences some adjustment at the outflow boundary likely as a result of the boundary conditions. The streamwise wavenumber obtained from the radial code is $\alpha = \alpha_r + i\alpha_i = 0.9984 - 0.0113i$. The phase speed is 0.23717 (Fig. 23b). The streamwise wavenumber, α_r, and spatial growth rate, α_i, are within 0.22 % and 3.67%, respectively, of the results reported by Chung et al.[32]

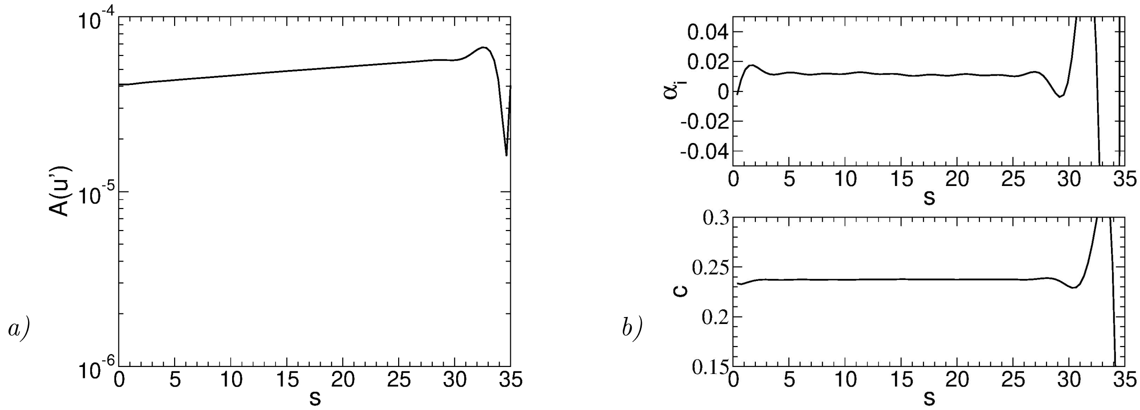

Figure 23. ***a)*** **Fourier modes of wall-normal disturbance velocity at mid-channel height and** ***b)*** **growth rates & phase speed vs. streamwise arclength for case 4.**

Conclusions

Similar to plane Rayleigh-Bénard-Poiseuille (RBP) flow, inward radial RBP flow can exhibit both buoyancy and viscosity-driven instability. The stability boundaries for plane RBP flow were first established by Gage and Reid.[7] For $Re < Re_c = 5,400$ and $Ra > Ra_c = 1,708$, buoyancy-driven instability occurs and 3-D waves are most unstable. On the other hand, viscosity-driven instability leads to the growth of Tollmien-Schlichting waves for $Re > Re_c$ and $Ra < Ra_c$. Although plane RBP flow attracted a lot of attention in the scientific community, the hydrodynamic instability of inward radial RBP flow is less well explored. This paper focuses on spatial stability simulations that were carried out with the intent to make a contribution to the physical understanding of inward radial RBP flows.

A new direct numerical simulation (DNS) code was developed for numerical stability investigations of radial RBP flows. First, a validation case with buoyancy-driven instability was considered. A very large inflow and outflow radius and narrow azimuthal extent were chosen such that effectively a plane channel flow was simulated. The spanwise wavelength of the most amplified wave was the same as in an earlier temporal stability simulation by the authors.[31] Next, the buoyancy-driven instability of a radial channel flow with much smaller inflow and outflow radius was investigated. For this case, the radial velocity increases almost hyperbolically in the streamwise direction. As the flow approaches the outflow, steady longitudinal waves with progressively lower azimuthal mode number experience maximum amplification. Buoyancy-driven instability also leads to the amplification of traveling oblique waves. However, the growth rate of the traveling waves decreases with increasing frequency. A simulation with spiral flow and buoyancy-driven instability was carried out as well. The growth rates were overall lower than for the radial flow. Interestingly, the simulation also indicated different relative wave angles and growth rates for the left and right traveling oblique waves. Finally, as a validation case with viscosity-driven Tollmien-Schlichting instability, the DNS results for plane Poiseuille flow by Chung et al.[32] were recomputed and matched with good accuracy.

Acknowledgments

This material is based upon work supported by the National Science Foundation under grant no. 1510179. The program manager is Dr. Ronald Joslin.

References

[1]Schlaich, J., "The Solar Chimney Electricity from the Sun," *Eds. F.W. Schubert and J. Schlaich, Edition Axel Menges, 1995, Deutsche Verlagsanstalt, Stuttgart*, 1994, C. Maurer, Geislingen, Germany

[2]Haaf, W., Friedrich, K., Mayr, G., and Schlaich, J., "Solar chimneys, part I: principle and construction of the pilot plant in Manzanares," *International Journal of Sustainable Energy*, Vol. 2, No. 1, 1983, pp. 3-22

[3]Haaf, W., "Solar chimneys, part II: preliminary test results from the Manzanares pilot plant," *International Journal of Solar Energy*, Vol. 2, 1984, pp. 141-161

[4]Schlaich, J., Bergermann, R., Schiel, W., and Weinerbe, G., "Design of commercial solar updraft tower systems-utilization of solar induced convective flows for power generation," *Journal of Solar Energy Engineering*, Vol. 127, 2005, pp. 117-124

[5]Miles, J.W., "On the stability of heterogeneous shear flows," *Journal of Fluid Mechanics*, Vol. 10, No. 4, 1961, pp. 496-508

[6]Pearlstein , A.J., "On the two-dimensionality of the critical disturbances for stratified viscous plane parallel shear flows," *Physics of Fluids*, Vol. 28, No. 2, 1985, pp. 751-753

[7]Gage, K.S., and Reid, W.H., "The stability of thermally stratified plane Poiseuille flow," *Journal of Fluid Mechanics*, Vol. 33, part I, 1968, pp. 21-32

[8]Mori, Y., and Uchida, Y., "Forced convective heat transfer between horizontal flat plates," *International Journal of Heat and Mass Transfer*, Vol. 9, No. 8, 1966, pp. 803-808

[9]Fujimura, K., and Kelly, R.E., "Stability of unstably stratified shear flow between parallel plates," *Fluid Dynamics Research*, Vol. 2, No. 4, 1988, pp. 284-292

[10]Reed, H.L., and Saric, W.S., "Linear stability theory applied to boundary layers," *Annual Review of Fluid Mechanics*, Vol. 28, 1996, pp. 389-428

[11]Bernardes, M.A.D.S., Valle, R.M, and Cortez, M.F.B., "Numerical analysis of natural laminar convection in a radial solar heater," *International Journal of Thermal Sciences*, Vol. 38, No. 1, 1999, pp. 42-50

[12]Ming, T., Liu, W., and Xu, G., "Analytical and numerical investigation of the solar chimney power plant systems," *International Journal of Energy Research*, Vol. 30, No. 11, 2006, pp. 861-873

[13]Ming, T.Z., Liu, W., Pan, Y., and Xu, G.L., "Numerical analysis of flow and heat transfer characteristics in solar chimney power plant with energy storage layers," *Energy Conversion and Management*, Vol. 49, No. 10, 2008, pp. 2872-2879

[14]Ming, T., Wang, X., de Richter, R.K., Liu, W., Wu, T., and Pan, Y., "Numerical analysis on the influence of ambient crosswind on the performance of solar updraft power plant system," *Renewable and Sustainable Energy Reviews*, Vol. 16, No. 8, 2012, pp. 5567-5583

[15]Pastohr, H., Kornadt, O., and Gurlebeck, K., "Numerical and analytical calculations of the temperature and flow field in the upwind power plant," *International Journal of Energy Research*, Vol. 28, No. 6, 2004, pp. 495-510

[16]Xu, G., Ming, T., Pan, Y., Meng, F., and Zhou, C., "Numerical analysis on the performance of solar chimney power plant system," *Energy Conversion and Management*, Vol. 52, No. 2, 2011, pp. 876-883

[17]Koonsrisuk, A., and Chitsomboon, T., "Effects of flow area changes on the potential of solar chimney power plants," *Energy*, Vol. 51, 2013, pp. 400-406

[18]Hu, S., Leung, D.Y.C., and Chan, J.C.Y., "Impact of the geometry of divergent chimneys on the power output of a solar chimney power plant," *Energy*, Vol. 120, 2017, pp. 1-11

[19]Van Santen, H., Kleijn, C.R., and Van Den Akker, H.E.A., "Mixed convection in radial flow between horizontal plates-I. Numerical simulations," *International Journal of Heat and Mass Transfer*, Vol. 43, No. 9, 2000, pp. 1523-1535

[20]Van Santen, H., Kleijn, C.R., and Van Den Akker, H.E.A., "Mixed convection in radial flow between horizontal plates-II. Experiments," *International Journal of Heat and Mass Transfer*, Vol. 43, No. 9, 2000, pp. 1537-1546

[21]Fasel, H., Meng, F., Shams, E., and Gross, A., "CFD analysis for solar chimney power plants," *Solar Energy*, Vol. 98, Part A, 2013, pp. 12-22

[22]Fasel, H.F., Meng, F., and Gross, A., "Numerical and Experimental Investigation of 1:33 Scale Solar Chimney Power Plant," 11th International Conference on Heat Transfer, Fluid Mechanics, and Thermodynamics, South Africa, 20-23 July 2015. URI: http://hdl.handle.net/2263/55874

[23]Bernardes, M.A.D.S., "Preliminary stability analysis of the convective symmetric converging flow between two nearly parallel stationary disks similar to a Solar Updraft Power Plant collector," *Solar Energy*, Vol. 141, 2017, pp. 297-302

[24]Sandberg, R.D., "Governing equations for a new compressible Navier-Stokes solver in general cylindrical coordinates," *Technical Report AFM-07/07*, University of Southampton, 2007. URI: http://www.eprints.soton.ac.uk/49523/

[25]Fan, P., "The standard upwind compact difference schemes for incompressible flow simulations," *Journal of Computational Physics*, Vol. 322, 2016, pp. 74-112

[26]Shukla, R.K., Tatineni, M., and Zhong, X., "Very high-order compact finite difference schemes on non-uniform grids for incompressible Navier-Stokes equations," *Journal of Computational Physics*, Vol. 224, No. 2, 2007, pp. 1064-1094

[27]Fyfe, D.J., "Economical Evaluation of Runge-Kutta Formulae," *Mathematics of Computation*, Vol. 20, No. 95, 1966, pp. 392-398

[28]Carlson, J.-R., "Inflow/outflow boundary conditions with application to FUN3D," *NASA/TM-2011-217181*, October 2011

[29]Gross, A., and Fasel, H.F., "Characteristic Ghost Cell Boundary Condition," *AIAA Journal*, Vol. 45, No. 1, 2007, pp. 302-306

[30]Hasan, M.K., and Gross, A., "Numerical Investigation of Hydrodynamic Stability of Inward Radial Rayleigh-Bénard-Poiseuille Flow," AIAA-Paper AIAA 2018-0586, 2018

[31]Hasan, M.K., and Gross, A., "Numerical Investigation of Rayleigh-Beńard-Poiseuille Instability of Plane Channel Flow," AIAA-Paper AIAA 2019-2320, 2019

[32]Chung, M.Y., Sung, H.J., and Boiko, A.V., "Spatial simulation of the instability of channel flow with local suction/blowing," *Physics of Fluids*, Vol. 9, No. 11, 1997, pp. 3258-3266